Phys Chem Minerals
DOI 10.1007/s00269-010-0410-3

ORIGINAL PAPER

Dislocation recovery in fine-grained polycrystalline olivine

R. J. M. Farla · H. Kokkonen · J. D. Fitz Gerald · A. Barnhoorn · U. H. Faul · I. Jackson

Received: 10 February 2009 / Accepted: 19 November 2010

Abstract The rate of static dislocation recovery in Fo_{90} olivine has been studied under conditions of high temperature and controlled atmosphere in compressively deformed polycrystals hot-pressed from synthetic (sol–gel) and natural (San Carlos) precursor powders. The sol–gel olivine, containing a small fraction of orthopyroxene, was deformed to a final strain of 19% with a maximum differential stress of 266 MPa whereas the San Carlos specimen was deformed to 15% strain and 260 MPa differential stress. Small samples cut from these deformed materials were annealed under high-temperature, controlled atmosphere conditions, for different durations to allow partial recovery of the dislocation sub-structures. Oxidative-decoration of the microstructural features, followed by back-scattered electron imaging at 5 kV and image analysis, was used to determine dislocation density. The variation of dislocation density ρ with time t at absolute temperature T was fitted to a second-order rate equation, in integral form, $1/\rho(t) - 1/\rho(0) = kt$ with $k = k_0 \exp(-E_a/RT)$. The activation energy E_a of the recovery process is 240 ± 43 and 355 ± 81 kJ mol^{-1} for sol–gel and San Carlos olivine polycrystals, respectively. The measured rates are one to two orders of magnitude lower than those reported in previous studies on natural single crystal olivine. The difference may be explained by several factors such as high dislocation densities measurable from large areas at high magnification for the SEM and the technique used to estimate dislocation densities. Comparison between fine-grained sol–gel olivine and the coarser-grained San Carlos olivine aggregate did not indicate that grain boundaries play an important role in dislocation recovery, but the absence of grain boundaries might also have contributed to the high dislocation recovery rates previously measured for single crystals.

Keywords Dislocation recovery · Sol–gel · San Carlos · Synthetic olivine · Microstructures · Diffusion · FE-SEM

Introduction

The rheological, diffusional, electrical and seismological properties of olivine, the most abundant mineral in the Earth's upper mantle, continue to be of primary interest for experimental research (Mei and Kohlstedt 2000; Karato and Jung 2003; Jackson et al. 2004; Du Frane et al. 2005; Dohmen et al. 2007; Spandler and O'Neill 2010). Much recent work has focussed on the use of pure polycrystalline iron-bearing olivine, $(Mg,Fe)_2SiO_4$, synthesized from laboratory reagents (Jackson et al. 2002; McDonnell et al. 2002; Faul and Jackson 2007). The benefit of using this synthetic equivalent to upper mantle rocks is the capability to work with polycrystals of controlled grain size and purity. However, using synthetic instead of natural material for experimental research requires re-examination of some of its material properties mentioned above. One important aspect was the evolution of dislocation configurations and

R. J. M. Farla (✉) · H. Kokkonen · J. D. Fitz Gerald · A. Barnhoorn · I. Jackson
Research School of Earth Sciences, Australian National University, Canberra, ACT 0200, Australia
e-mail: robert.farla@anu.edu.au

Present Address:
A. Barnhoorn
Department of Earth Sciences, Utrecht University, 3508 TA Utrecht, The Netherlands

U. H. Faul
Department of Earth Sciences, Boston University, Boston, MA 02215, USA

Published online: 05 December 2010

dislocation recovery kinetics in olivine during static recovery at high temperature.

Climb-controlled annihilation of dislocations operates as pairs of dislocations with opposite Burgers vectors meet via the diffusion of vacancies. The conditions favourable for dislocation climb occur at medium to high temperatures ($T > 0.4\ T_m$). Dislocations can also anneal via cross-slip, which occurs as a stress-assisted process at high temperatures (Poirier and Vergobbi 1978). Not all dislocations annihilate during recovery. Some dislocations glide and climb into stable positions in the crystal lattice leading, for example, to the formation of dislocation tilt walls. Overall, these recovery processes lead to a reduction in the free dislocation density, particularly during static recovery.

Dislocation recovery is dependent on many factors including temperature, pressure, chemical environment and the duration of annealing. Several studies on dislocation recovery have been carried out on natural olivine single crystals (Kohlstedt et al. 1980; Karato and Sato 1982; Bai and Kohlstedt 1992; Karato et al. 1993; Karato and Jung 2003), but none so far have examined polycrystalline material derived from sol–gel and San Carlos olivine precursors. These two types of materials were deformed and annealed, and large areas of transverse sections were analysed using the latest high resolution scanning electron microscope (SEM) imaging techniques. This study offers a systematic method for determining the true dislocation line lengths and hence the true dislocation density measured in a volume of material. The results offer a solid prediction for reduction of dislocation density (free dislocations) in sol–gel and San Carlos olivine for different temperatures and annealing times. The recovery rate of dislocations was calculated to determine the activation energy and the process controlling the rate of dislocation recovery. Some constraints on the dislocation recovery mechanisms were evaluated.

Experimental procedure

Fully synthetic dry iron-bearing (Fo_{90}) olivine has been prepared via a solution–gelation (sol–gel) method detailed in studies by (Jackson et al. 2002; Faul and Jackson 2007). Fe and Mg nitrates and tetraethyl orthosilicate (TEOS) were dissolved in an ethanol solution. Gel formation resulted from a change in pH and slow heating above room temperature. A series of steps followed including the dehydration of the gel, cold pressing, firing and grinding of olivine pellets at different temperatures and f_{O_2}. The last firing was done at 1,400°C and f_{O_2} of 7×10^{-10} bar. To reduce the porosity, a stack of several fired pellets was wrapped in a $Ni_{70}Fe_{30}$ foil, loaded in a steel jacket and hot pressed at 1,300°C and 300 MPa confining pressure for 24 h. The resulting cylindrical specimen was a dense olivine aggregate of 2.7×10^{-6} m mean grain size with 12% orthopyroxene (opx) as silica buffer and <1% porosity (specimen #6532 of Faul and Jackson 2007). The hot-pressed specimen was ground to cylindrical shape and fired at 1,200°C. It was subsequently compressively deformed at 1,250°C and 300 MPa Ar confining pressure up to 266 MPa differential stress. Total strain in the specimen after deformation was about 19% (Faul et al. 2010). The deformed specimen was recovered and transversely sectioned. Small 2 mm by 2 mm cubes were cut and mounted in epoxy for polishing in anticipation of the annealing experiments.

The San Carlos olivine samples were similarly prepared for annealing experiments. Inclusion-free grains were hand-picked from a suite of San Carlos olivine phenocrysts under the light microscope (see Tan et al. 2001). The grains were crushed, sieved and further size sorted by sedimentation from suspension to separate out the 10×10^{-6} to 38×10^{-6} m grain size fraction. Pellets were cold pressed from the resulting San Carlos powders and given the same treatment of firing and hot pressing until a long cylindrical sample was prepared for compressive deformation. It was deformed at 1,250°C and 300 MPa Ar-confining pressure (run #6701) to 15% strain at 260 MPa differential stress. Likewise, a 2-mm slice was cut from one end of the cylindrical sample from which the annealing samples were prepared.

The dislocation recovery experiments were performed at temperatures of 1,100–1,500°C and annealing times of 3–50 h under controlled oxygen fugacity conditions at atmospheric pressure utilising CO and CO_2 gas flow controllers. The oxygen fugacity and temperature were monitored in real time with an oxygen sensor and a thermocouple respectively and logged for the duration of the experiment. The f_{O_2} conditions were chosen to simulate the conditions during planned seismic wave attenuation experiments for which the specimen will be wrapped in an $Ni_{70}Fe_{30}$ foil (Jackson et al. 2002). Hence, a fixed mixture of 70% CO and 30% CO_2 approximating the $Ni_{70}Fe_{30}$–Fo_{90} olivine redox buffer was used in all experiments, unless otherwise indicated. This consideration was judged to be more important than isolating the effect of the oxygen fugacity on the rate of dislocation recovery as investigated by Karato and Sato (1982) where a slight negative trend was resolved but with large uncertainty. The oxygen sensor reported consistent f_{O_2} readings for the duration of the annealing experiments, which match the calculated f_{O_2} values within 0.2 log units. For each annealing run, an olivine sample was placed in a platinum cup fitted with a grid of thin platinum wires on the bottom to ensure minimal contact with the cup and therefore minimal iron loss.

The temperature was ramped up at rates varying from 12 up to 50°C/min for higher target temperatures (≥1,250°C). After a specified dwell time at the target temperature, the furnace was quenched at an estimated rate of 50°C/min to prevent any further dislocation recovery during cooling. Although this cooling rate was relatively slow, it was decided not to quench samples more rapidly in water in order to avoid major cracking and/or the generation of new dislocations. As a result, significant levels of dislocation recovery would have occurred during the comparatively long ramp times and these must be taken into account particularly for the shortest experiments (0.5–5 h). The emerging constraints on the temperature dependence of the dislocation recovery rate allowed a correction for this effect.

The continuous temperature ramps were approximated as 50°C steps. Time spent at steps 0–1,100°C was ignored, based on the observation that dislocation recovery rate was unmeasurable at such temperatures. Taking 50°C/min for heating and cooling ramp rates, positive corrections to the final dislocation density were made for $T \geq 1{,}250$°C for sol–gel olivine, exceeding 0.4%, as follows: 1,350°C (0.45%), 1,400°C (0.71%), 1,450°C (1.10%). For San Carlos olivine these corrections are: 1,350°C (0.94%), 1,400°C (1.91%), 1,450°C (4.20%), 1,500°C (8.27%). Note that the number of dislocations that anneal during heating will be larger than the number of disappearing during cooling. This was taken into account by approximating the final dislocation density of the samples as the initial dislocation density in order to calculate the correction during cooling. The San Carlos corrections were greater due to a higher dislocation recovery rate at high temperature.

Imaging and determination of dislocation density

The decoration of dislocations was performed using a variation on the oxidative-decoration technique initially developed by Kohlstedt et al. (1976) and later used with the SEM by Karato (1987). Earlier dislocation recovery studies, (Durham et al. 1977; Kohlstedt et al. 1980; Karato and Ogawa 1982) used the oxidative-decoration technique for light microscope (LM) imaging. Our samples were prepared for field emission scanning electron microscope (FE-SEM) imaging by grinding about 80×10^{-6} m from the surface of the annealed specimen using silicon carbide, thereby removing any surface contamination. The grinding was followed by a fine polish with a 0.05×10^{-6} m alumina slurry. The polished surfaces were then oxidised at 900°C for 45 min. After oxidation, another polish was performed for 10 min using the same alumina slurry, previously determined to guarantee the best result. The iron-oxide surface coating was removed ($<1 \times 10^{-6}$ m) and the most decorated region of dislocations was about $2–6 \times 10^{-6}$ m deep. The samples were cleaned and observed under the LM at the highest magnification (1,000×) to check that the grain boundaries and dislocations are clearly visible.

The Hitachi 4300 SE/N FE-SEM was used to image the decorated dislocations at an acceleration voltage of 5 kV. Working distance used was 10 mm, the condenser lens was set at 6 (equivalent to $\sim 10^{-10}$ A specimen irradiation current), aperture was set to 100×10^{-6} m, the emission current was 43×10^{-6} A, the imaging current was about 0.4×10^{-9} A and gun brightness was set to 3. Images of 2,048 × 1,536 pixels were captured in a rectangular grid pattern. In order to establish optimal imaging conditions for dislocation density measurements, selected regions were imaged at different magnifications. From 3,000× to 8,000× magnification, the apparent dislocation density increased by 75% as a higher magnification allowed previously overlapping dislocations to be resolved into distinct lines. Beyond 8,000× there was little change. So this magnification was used for all subsequent dislocation density measurements.

The FE-SEM images were prepared for dislocation density measurements using public domain software called ImageJ (http://rsbweb.nih.gov/ij/). Several stages in the procedure are shown in Fig. 1. High contrast images (Fig. 1a) were inverted (Fig. 1b) and processed with a threshold filter. The threshold operation converts a grey-scale image to a binary image (Fig. 1c) and the threshold value was manually adjusted to produce sharp dislocation images which remained continuous. This adjustment was required because, despite care taken to impose standard imaging conditions, fluctuations in the electron beam produced slightly different image brightness and contrast levels between weekly sessions. Two noise filters were used to remove all groups of five or fewer pixels. Such small clusters of pixels were not considered to be representative of dislocations but rather specks of contamination on the sample surface for instance.

In the process of distinguishing individual dislocations from other features, in this study dislocation walls were excluded. Walls were identified either as relatively long, often straight, solid lines crossing a grain or as arrays of solitary dislocations. The dislocations were highlighted using a colouring tool (Fig. 1d) and all other structures (e.g. grain boundaries, dislocation walls, pores, etc.) were removed using a colour filter (Fig. 1e). Lastly, the porosity and opx grains were manually highlighted and their areas subtracted from the total area to be counted (Fig. 1f).

From such processed images containing only free dislocations, dislocation density was estimated by invoking an add-on called 'Bézier curve ROI' for imageJ (http://www.optinav.com/Measure-Roi.htm). It fits a parametric curve to the end points of an object and any undulations in

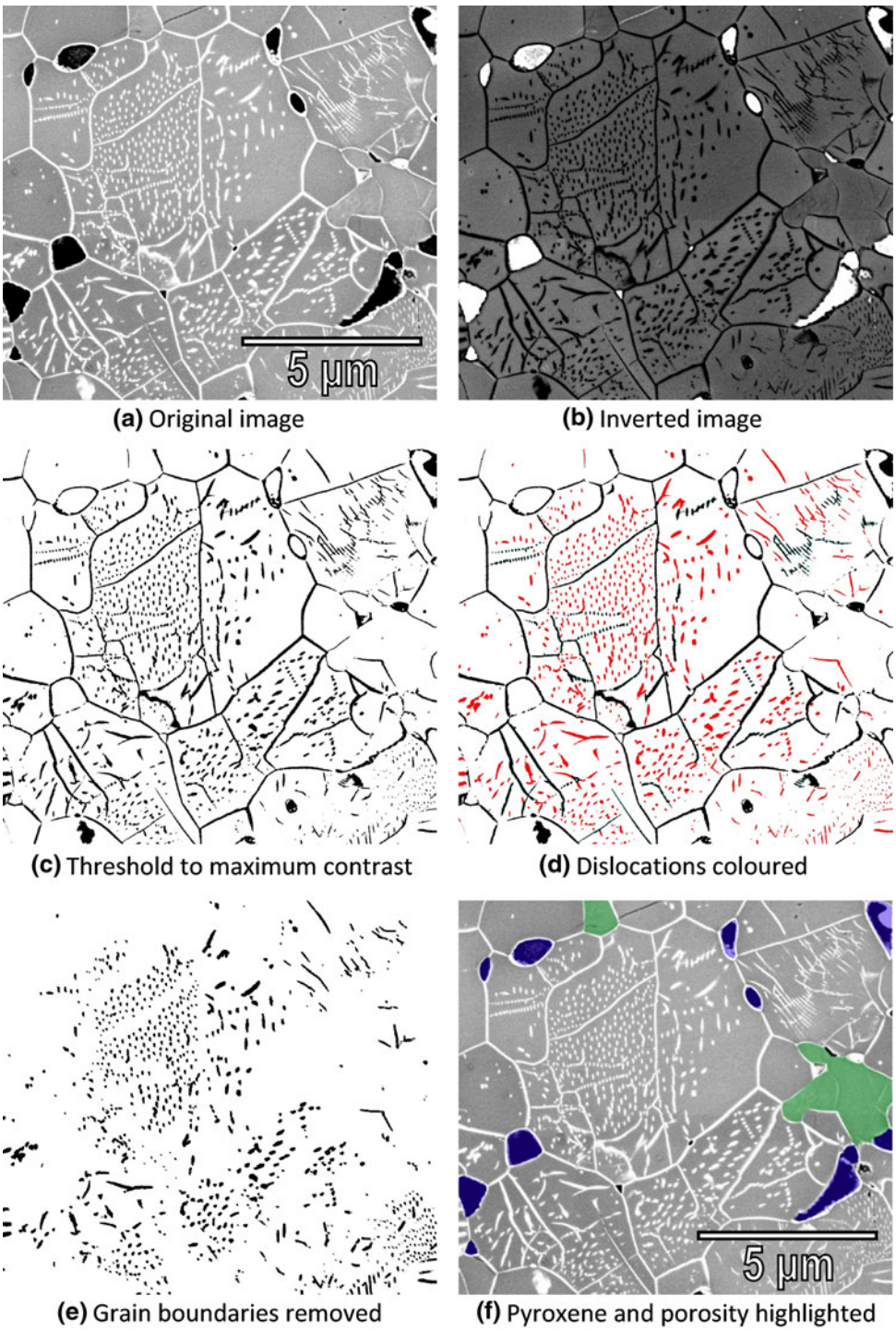

Fig. 1 Procedure for obtaining the uncorrected 2D dislocation density of the as-deformed olivine specimen. **a**–**e** show how the original SEM image was inverted, processed with a contrast filter of an appropriate threshold, manually coloured with a colour replacement tool so that a colour threshold filter can be applied to remove the grain boundaries. f shows the manual highlighting of the porosity (*dark blue*) and pyroxene grains (*green*) that were excluded from the calculated area. To get the 3D dislocation density result, the line lengths were measured in **e** instead of the number of dislocations (see Eq. 1)

between. This way, the 'projected' length of every individual dislocation was calculated—the sum of which gives the cumulative length of all dislocations.

The 'projected' dislocation length was important to know, because the dislocation density can be quantified in two ways. The first method involves counting the number of dislocations N imaged. When the number of dislocations was divided by the area, the uncorrected two-dimensional (2D) dislocation density was obtained (see Fig. 2a). However, dislocations are line defects and hence the 'true' dislocation density should be estimated by measuring the cumulative length of dislocation lines and dividing by the volume. This was referred to as the three-dimensional (3D) dislocation density, considered to be more accurate than a simple dislocation count over an area. It has previously been suggested that the 3D dislocation density might be

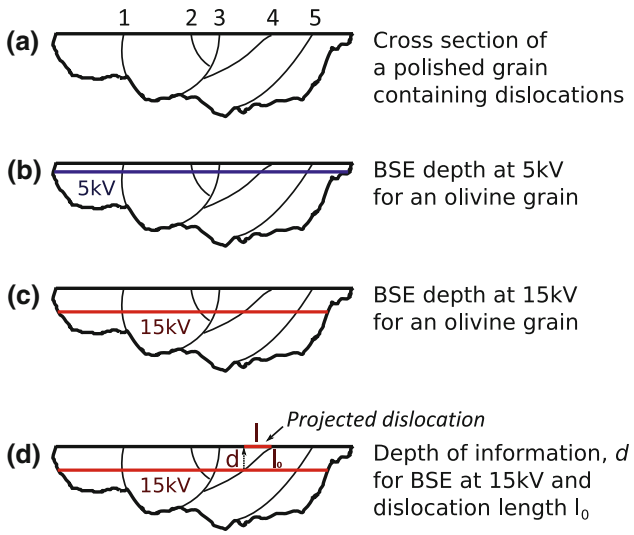

Fig. 2 Method used to determine the depth of information, d and hence the true dislocation line length, l_0. **a** The uncorrected 2D dislocation density was determined by counting the number of dislocations over an area. **b**, **c** d is more shallow with a lower accelerating voltage. **d** l_0 was determined from d and l, respectively

approximated by $\rho_{3D} = 2N/A$ (see "Comparison with other work") (Karato 2008).

To obtain the 3D dislocation density from the FE-SEM images, the true dislocation line length l_0 must be calculated from the projected length l and the depth of information d. This depth is not the electron penetration depth (see Appendix), but rather the depth from which backscattered electrons (BSEs) were returned to the backscatter detector situated above the sample. Figure 2 highlights the difference between using different accelerating voltages and how l_0 was calculated. In this study, $d = 0.095 \times 10^{-6}$ m was used at 5 kV (see Appendix). The 3D dislocation density was calculated as the sum of l_0 over the volume of material (area times d) expressed as

$$\rho_{3D} = (1/A) \sum \left[\sqrt{1 + (l/d)^2} \right] \quad (1)$$

where A is the total area imaged.

Total areas imaged for each dislocation density measurement were around $4{,}000 \times 10^{-12}$. Up to four such areas were measured per sample. The uncertainty in the data was obtained by dividing the total area imaged per sample into small areas each of about $300-500 \times 10^{-12}$ m^2. The dislocation density was then calculated as the mean of those for all areas. The standard error was given by twice the standard deviation over the square root for the total number of measurements. Error propagation was used to carry the uncertainty from the dislocation density into the recovery rate. Relatively larger errors towards lower temperature reflect the small differences between the initial and final dislocation densities.

Alongside characterizing FE-SEM images for dislocations, a lower magnification (1,000×) light microscope was also used in this study. Thin sections of two oxidised samples from the San Carlos olivine samples were prepared, one from the as-deformed material and the other from a sample annealed at 1,200°C. Four areas, each $6{,}640 \times 10^{-12}$, were analysed per sample. Dislocations were then hand traced and counted to produce uncorrected 2D dislocation densities for the deformed and annealed sample (SC-06). The 3D dislocation density, from the light microscope images, was calculated using the thickness of the thin section, determined by focusing successively on the top and bottom surface of the section. The difference in focal position multiplied by the value of the refractive index of Mg-rich olivine (~ 1.65) yields the thickness of the thin section—confirmed by the birefringent colours of olivine throughout the section.

The grain size of the original deformed sol–gel sample #6532 was determined from the FE-SEM images (as shown in Fig. 1a). Unfortunately, the grain boundaries can be discontinuously decorated by oxidation creating potential for two or more grains to be counted together, in some instances, leading to an overestimation of the grain size. Therefore, the grain boundaries were hand traced to ensure accurate grain size determination. The grain size of the original deformed San Carlos sample #6701 was determined via electron backscatter diffraction (EBSD). The images containing grain size information were processed using ImageJ which can treat single grains as particles. The area of every grain was measured and the equivalent diameter was determined. A correction (multiplication by a factor $4/\pi$, see Jackson et al. 2002) was applied to account for sectioning bias.

Recovery kinetics

There are a number of equations that describe particular recovery mechanisms based on distinct rate-limiting steps. These recovery mechanisms include diffusion-controlled dislocation glide, dislocation cross-slip, dislocation climb controlled by vacancy bulk diffusion or core diffusion or solute drag. The rate of dislocation recovery by dislocation glide, climb or cross slip can be expressed as

$$\sqrt{(\rho_f/\rho_i)} = [1 + t/\tau]^{-m} \quad (2)$$

where ρ_i and ρ_f are the initial and final dislocation densities, respectively. τ is a relaxation time parameter containing an Arrhenius term involving the activation energy for diffusion or cross slip. In Eq. 2, $m = 1$ for dislocation glide recovery with lateral jog drift, $m = 1/2$ for climb controlled by vacancy bulk diffusion, $m = 1/4$ for climb controlled by vacancy core diffusion and $m = -1$ for cross

slip (Nes 1995). The equation was based on quantifying the growth of the network of increasingly widely spaced dislocations and jogs.

Alternatively, one can express dislocation recovery kinetics empirically using the general nth-order dislocation recovery rate equation

$$\frac{d\rho}{dt} = -\rho^n k \tag{3}$$

where k is the rate constant. This integrates for $n \neq 1$ to

$$1/\rho_f^{n-1} - 1/\rho_i^{n-1} = kt(n-1) \tag{4}$$

and for $n = 1$ to

$$\rho_f/\rho_i = e^{-kt} \tag{5}$$

The rate constant k is given by

$$k = k_0 \exp\left(\frac{-E_a}{RT}\right) \tag{6}$$

where E_a is the activation energy for dislocation recovery, R is the gas constant, T is the temperature and k_0 is a constant.

Results

Dislocation microstructures

Overall, there was no significant increase in grain size through prolonged high temperature annealing, indicating a stable grain-scale microstructure for both the sol–gel and San Carlos olivine samples. The average grain size for the deformed sol–gel olivine specimen is $(3.8 \pm 0.2) \times 10^{-6}$ (795 grains) and $(13.0 \pm 0.47) \times 10^{-6}$ m (1,275 grains) for deformed San Carlos olivine. The porosity ranges from 2 to 3% for the deformed and annealed sol–gel samples except for the highest temperature annealing (1,400°C), which caused an increase in porosity to as much as 14% throughout the sample. The same occured at very high temperature in the coarser grained annealed San Carlos samples but was less pronounced, except at the edges of the samples. The porosity was generally between 2 and 3% but for samples SC-02 and SC-01 (at 1,450 and 1,500°C) porosity increased to 5% in the central region.

Figure 3 shows the typical arrangements of dislocations before (a) and after annealing (b,d) in sol–gel olivine. Dislocation density was significantly lower in the annealed samples and the grain boundaries appear to have straightened as well. Figure 3a shows that most grains contain a large concentration of dislocations with some preferential azimuthal orientation within each grain. Dislocation alignment was more pronounced after annealing at high temperature (Fig. 3b). Figure 3d shows that most dislocations have been annihilated with the remainder having moved into stable sub-structures. A few olivine grains contain almost no dislocations. The opx grains were generally dislocation-free, possibly the result of high temperature phase transformation. Figure 3c shows a large olivine grain with a high dislocation density typical of the deformed San Carlos specimen. The initial dislocation density for San Carlos is $(11.4 \pm 2.9) \times 10^{-12}$ m^{-2}, a little higher than that for sol–gel olivine of $(8.5 \pm 0.9) \times 10^{-12}$ m^{-2}.

When observing isolated dislocation segments inside grains one must keep in mind that the imaged area is a representation of a 3D microstructure. Individual dislocation lines must terminate at an impurity, pore space, grain boundary or another dislocation. However, the depth of information at 5 kV was sufficiently low (see Appendix) that only the near-surface parts of plunging dislocations can be seen. Dislocation walls as seen in Fig. 3 are less abundant in the sol–gel material (both deformed and annealed) than in the San Carlos samples with larger grain size (e.g. Fig. 3c for a large grain in the as-deformed San Carlos specimen).

Information concerning the slip plane and direction of slip for dislocations cannot be determined from the FE-SEM images.

Dislocation recovery rate

The initial dislocation density ρ_i, measured on each of the deformed specimens, was found to be uniform within experimental error for sufficiently large areas (Tables 1 and 2). These values of ρ_i, in combination with those (ρ_f) measured on the annealed specimens, were used to calculate the second-order rate constant k (Eq. 4) with $n = 2$. The rate constants thus estimated for the sol–gel and San Carlos olivines are presented in Tables 1 and 2, respectively, and those based on the 3D dislocation densities are plotted against reciprocal absolute temperature in Fig. 4. Note that the 3D dislocation densities reported here are comparable to values measured in similar polycrystalline olivine (Karato and Jung 2003) but are higher by one order of magnitude compared to single crystal olivine measurements (Durham et al. 1977; Karato and Ogawa 1982; Karato et al. 1993). As has been customary in such studies (Kohlstedt et al. 1980; Karato and Ogawa 1982), we have used the second-order rate law—as appropriate for recovery by dislocation–dislocation annihilation. The physical reason for choosing a second order rather than first order rate law is that second order kinetics imply dislocation-dislocation annihilation rather than dislocation adsorption at grain boundaries, a process which would be described by first order kinetics. The former, rather than the latter was believed to have occurred judging from microstructural

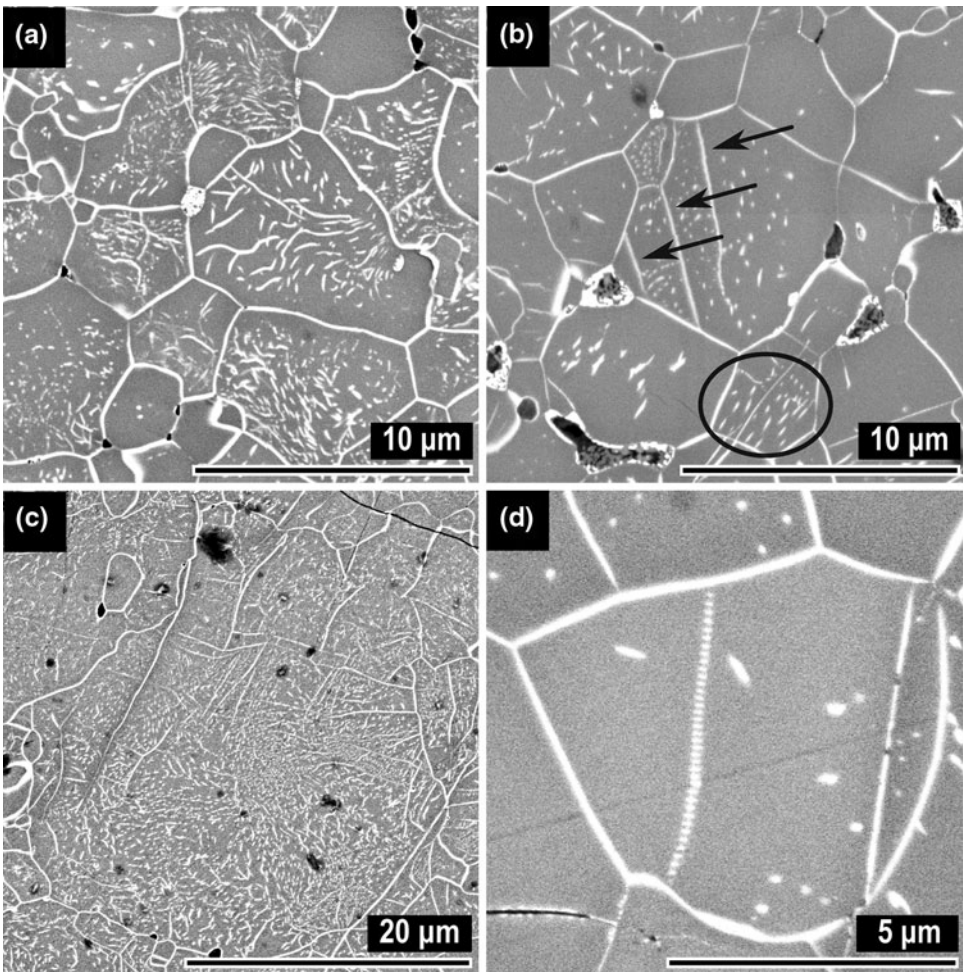

Fig. 3 **a** Backscattered image of a section of the deformed sol–gel olivine. **b** Backscattered image of the same material after annealing at 1,300°C for 50 h. *Arrows* indicate dislocations organised into walls. The *circle* indicates a region with many parallel dislocation lines. **c** A typical grain in the San Carlos olivine packed with closely spaced dislocations prior to annealing. **d** Example of a dislocation tilt wall sub-structure after annealing at high temperature with dislocations separated by just 130×10^{-9} m

Table 1 Summary of recovery experiments on sol–gel olivine

Specimen[a]	T (°C)	f_{O_2} (10^{-6} Pa)	t[b] (h)	2D ρf[c] (10^{12} m^{-2})	3D ρf[d] (10^{12} m^{-2})	Recovery (%)	log (k, m^2 s^{-1})[e]
Fo-01	1,450	75	3	0.6	4.1 ± 0.6	51 ± 8	−16.95
Fo-02	1,400	23	3	1.2	5.1 ± 0.6	40 ± 9	−17.14
Fo-03	1,350	6.4	3	1.7	6.4 ± 0.7	24 ± 11	−17.46
Fo-04	1,300	1.7	3	2.2	6.5 ± 0.8	23 ± 12	−17.49
Fo-05	1,300	1.7	8	1.7	5.6 ± 0.7	34 ± 10	−17.71
Fo-06	1,300	1.7	16	1.5	5.0 ± 0.5	41 ± 8	−17.86
Fo-07	1,300	1.7	50	1.7	3.5 ± 0.6	59 ± 8	−18.02
Fo-08	1,200	0.086	50	1.4	3.9 ± 0.4	54 ± 6	−18.13
Fo-08[f]	1,200	1.7	50	1.3	4.0 ± 0.4	53 ± 7	−18.11
Fo-09	1,100	0.0029	50	2.7	7.1 ± 0.5	16 ± 10	−18.90

[a] Average grain size after deformation is $(3.8 \pm 0.2) \times 10^{-6}$ m

[b] Time at maximum temperature. Corrections to k were made for the duration of heating and cooling ramps (see text)

[c] Final 2D dislocation density (with $\rho_i = \sim 2.8 \times 10^{12}$ m^{-2})

[c] Final 3D dislocation density (with $\rho_i = (8.5 \pm 0.9) \times 10^{12}$ m^{-2})

[e] Rate constant, k based on 3D dislocation density calculation

[f] Annealing experiment carried out away from the $Ni_{70}/Fe_{30} - Fo_{90}$ buffer

Table 2 Summary of recovery experiments on San Carlos olivine

Specimen[a]	T (°C)	f_{O_2} (10^{-6} Pa)	t[b] (h)	2D ρf[c] (10^{12} m^{-2})	3D ρf[d] (10^{12} m^{-2})	log (k, m^2 s^{-1})[e]
SC-01	1,500	230	0.5	1.3	3.7 ± 0.6	−16.05
SC-02	1,450	75	1	1.4	4.0 ± 0.9	−16.38
SC-03	1,400	23	2	1.4	3.4 ± 1.6	−16.56
SC-04	1,350	6.4	5	1.9	4.8 ± 1.2	−17.19
SC-05	1,300	1.7	16	1.5	3.6 ± 1.1	−17.49
SC-06	1,200	0.086	20	3.4	7.9 ± 1.8	−18.27
SC-07	1,100	0.0029	50	4.1	9.1 ± 1.2	−18.90

[a] Average grain size after deformation is (13.0 ± 0.47) × 10^{-6} m

[b] Time at maximum temperature. Corrections to k were made for the duration of heating and cooling ramps (see text)

[c] Final 2D dislocation density (with $\rho_i = \sim 5.2 \times 10^{12}$ m^{-2})

[c] Final 3D dislocation density (with $\rho_i = (11.4 \pm 2.9) \times 10^{12}$ m^{-2})

[e] Rate constant, k based on 3D dislocation density calculation

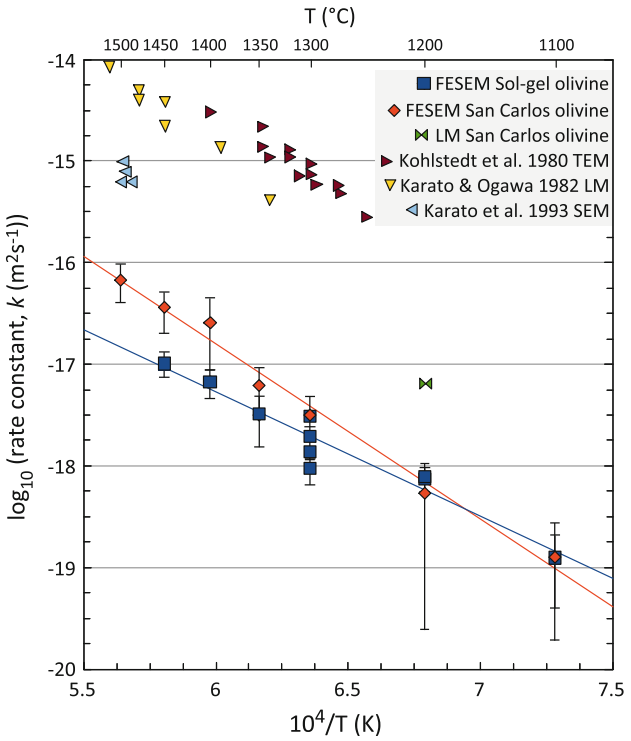

Fig. 4 Rate constant versus the reciprocal of temperature (3D calculation, Tables 1 and 2). Light Microscope data; Karato and Ogawa (1982), Karato et al. (1993) and this study. TEM data; Kohlstedt et al. (1980) and Karato et al. (1993). SEM data; Karato et al. (1993). All previous studies used San Carlos single crystals. FE-SEM data; this study (polycrystalline sol–gel and San Carlos olivine). All the data were obtained under atmospheric pressure. A linear regression line was fitted to each of the data sets from this study

observations. Conveniently, the second-order rate constant has the same unit as the diffusivity (m^2 s^{-1}), facilitating a comparison between the two quantities.

Broadly similar recovery rates for sol–gel (E_a = 240 ± 43 kJ mol^{-1}, k_0 = 1.73 × 10^{-10} m^2 s^{-1}) and San Carlos olivine (355 ± 81 kJ mol^{-1}, k_0 = 1.85 × 10^{-6} m^2 s^{-1}) are presented with some divergence at high temperature, for a larger activation energy for San Carlos olivine (Fig. 4). The uncertainty reflects both errors in the data and the scatter of the data about the optimal model. The four data points for the sol–gel at 1,300°C are measurements for different annealing durations (3, 8, 16, 50 h). The two overlapping data points at 1,200°C and 50 h annealing are for different CO/CO_2 gas mixes and therefore different oxygen fugacity. While there may be an effect of the oxygen fugacity on the dislocation recovery rate, it was not measured in this study. However, f_{O_2} was only varied by a factor of 20. The lone data point (green) was obtained from a light microscope study of the decorated San Carlos samples (deformed and annealed, SC-06) and indicates a significantly higher 'apparent' rate constant.

Figure 5 provides a complementary view of the same data and the second-order recovery model for the sol–gel olivine specimen. The percentage of recovery was calculated for this model based on parameter values for k_0 and Ea determined via Fig. 4. Each dashed curve represents a particular duration of annealing. This figure highlights the implications of the dislocation recovery model for the stability of dislocation microstructures during prolonged high-temperature testing.

The two data points at 1,200°C ($10^4/T$ = 6.8) and 50 h in Fig. 5 are those measured at different oxygen fugacity levels (Fo-08 and Fo-08* in Table 1). For the data point closer to the 50 hour curve the gas mixture was varied to achieve the same f_{O_2} as for the data point at 1,300°C. All other data were obtained under f_{O_2} conditions given by a constant gas mix of 70% CO/30% CO_2. The 1,200°C results have been taken to demonstrate that the effect of f_{O_2} was small enough to be within the uncertainty of the measurements (of about 0.1 × 10^{-14} m^2 s^{-1} for 1.3 orders of magnitude difference in oxygen fugacity).

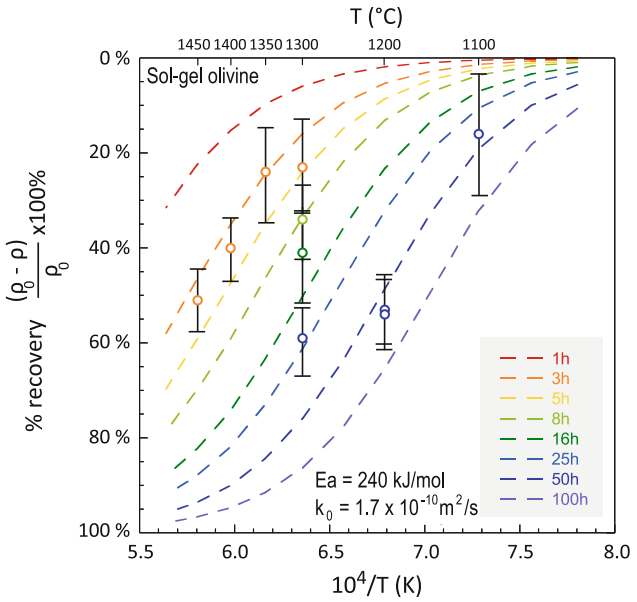

Fig. 5 Percent recovery versus the reciprocal of temperature. The annealing time is indicated with a *different colour* for each curve (calculated via Eq. 6). Each data point is correspondingly *colour coded* accordingly to its annealing time. All the data were obtained under atmospheric pressure only

Uncertainty in measured dislocation density

High dislocation density leads to overlapping dislocations that make counting difficult (although this was improved for imaging at 5 kV relative to higher accelerating voltages) and increases uncertainty in dislocation density measurements. In addition, scatter in the data results from the heterogeneity in the dislocation distribution between grains. Figure 3a, for example, shows a representative area where a few grains contain no dislocations. The proportion of dislocation-free grains increases with increasing dislocation recovery at higher temperature, thereby enhancing the uncertainty in the data (see Fig. 4).

This study found that larger areas for dislocation measurements provide more robust results but come at the cost of more time and resources. During an initial calibration, where the dislocation density was measured over different areas at a constant magnification of 8,000×, it was found that the dislocation density for total areas of 10,000 to 20,000 $\times$ 10^{-12} m^2 did not significantly change. However, dislocation density measurements for areas down to 500 $\times$ 10^{-12} m^2 show a variability in dislocation density to more than $\pm 2 \times 10^{12}$ m^{-2}.

As a final check on image processing using the various contrast filters, dislocations in one grain were counted manually at 11,000× magnification on a raw image. The dislocation density using the method described earlier at 8,000× was about 15% less than the manual recount, comparable with the statistical uncertainty of 7–18% in Table 1, therefore the tabulated results may be a slight under-estimate, but acceptable given the practical limitation that twice as many images need to be processed for 11,000× magnification. This slight increase in dislocation density will not yield a statistically significant decrease in the rate constant.

Discussion

Dislocation microstructures

The deformed fine grained sol–gel olivine (and to a lesser extent San Carlos olivine) shows some grains devoid of dislocations even before annealing. These grains may have been in an orientation unfavourable for internal deformation by dislocation creep, reducing the number of generated dislocations. Hence, it cannot be said with certainty whether annealing can allow the elimination of all dislocations from a grain.

The presence of isolated dislocation walls after high temperature annealing suggests that these were stable sub-structures unlikely to undergo further recovery (see Fig. 3d). Dislocation walls may act as attractors for annihilation of free dislocations of opposite sign, especially if these sub-structures develop early on during recovery or have already formed via dislocation creep during deformation. Figure 3b, however, shows several isolated dislocations persisting in the region between dislocation walls after 50 h at 1,300°C. Occasionally, a network of dislocation walls was observed in the annealed samples. Individual dislocations in walls can be resolved at the highest magnification of the FE-SEM in some rare cases. Typically, the BSE image quality does not improve beyond 20,000× magnification. Dislocations making up these walls were typically less than 50 nm apart. More widely spaced dislocations occur in walls that must be of lower misorientation angle. Dislocation wall structures indicate recovery and reorganisation of dislocations during annealing. When the spacing between dislocations in a dislocation structure becomes too small, it becomes indistinguishable from a grain boundary in the backscattered images. As mentioned before, such structures were not included in the dislocation density estimation.

Figure 3b demonstrates some other dislocation sub-structures which were not seen in the original deformed material. The observable decrease in the average number of curved dislocations between Fig. 3a (e.g. centre grain), 3b and 3d in statically annealed samples gives an indication of significant dislocation climb (Lui and Evans 1997).

Comparison with other work

The dislocation density measured in this study was of the order of 10^{12}–10^{13} m^{-2} (Tables 1 and 2). This is generally up to one order of magnitude higher than in deformed single crystal olivine on which dislocation recovery studies were carried out (Kohlstedt et al. 1980; Karato and Ogawa 1982; Karato and Sato 1982; Karato et al. 1993), but comparable to results from rheology studies on deformed polycrystalline olivine of broadly similar grain size (Jung and Karato 2001; Karato 2003).

In Fig. 4, the rate constant $k = (1/\rho_f - 1/\rho_i)/t$ calculated from the change in dislocation density for both sol–gel and natural San Carlos polycrystalline olivine is lower by 1–2 orders of magnitude than for single crystal San Carlos olivine (Fo_{92}) from a LM study by Karato and Ogawa (1982) and a single crystal TEM study by Kohlstedt et al. (1980). k is lower by over one order of magnitude compared to a small set of data obtained by Karato et al. (1993) for single crystal San Carlos olivine.

The activation energy calculated for dislocation recovery in single crystal San Carlos olivine is 398 ± 59 kJ mol^{-1} (Karato and Ogawa 1982), which compares quite well with that for polycrystalline olivine determined over a wider temperature range in this study (355 ± 81 kJ mol^{-1} for San Carlos olivine and 240 ± 43 kJ mol^{-1} for sol–gel olivine). A much higher value of 586 ± 126 kJ mol^{-1} for a natural deformed peridotite was obtained by Goetze and Kohlstedt (1973), not plotted in Fig. 4. For the study of single crystal San Carlos olivine by Karato et al. (1993) no activation energy was obtained but Kohlstedt et al. (1980) obtained a value of 328 ± 31 kJ mol^{-1} and Yan (1992) obtained an activation energy of 219 kJ mol^{-1} using natural olivine.

The dislocation density for other studies was obtained using different techniques. The LM was used for imaging in the study by Karato and Ogawa (1982). The LM has the limitation that it can image only up to a magnification of 1,000× and therefore with a high dislocation density, many dislocations were potentially missed. TEM imaging carried out by Kohlstedt et al. (1980) was done at high magnification (10,000×) but only on small areas (24 times 54×10^{-12} m^2), complicating the determination of a robust average for a markedly heterogeneous dislocation distribution. In none of the previous studies was the 3D dislocation density estimated via measurement of dislocation line lengths. However, such a correction was not necessary when dislocations were imaged end-on (as in suitably oriented single crystals; Karato et al. 1993).

The San Carlos polycrystal of the present study has a larger grain size than the sol–gel olivine and may likely contain higher concentrations of trace elements due to its natural origin. However, we measured a recovery rate broadly consistent with that of sol–gel olivine. Only at high temperatures is k systematically different indicating a somewhat more strongly temperature dependent rate constant for San Carlos olivine.

Since a similar recovery rate was observed for olivine of larger grain size, prepared from the natural precursor, a further measurement was performed based on images recorded in a petrographic light microscope. Uncorrected 2D dislocation analysis of the thin section photos using the hand trace method described in section 1 produced dislocation densities of 8.0×10^{10} and 7.7×10^{10} m^{-2}, respectively, for the deformed and annealed sample, SC-06 with k equal to 5.6×10^{-18} m^2 s^{-1} (see plotted value in Fig. 4). Calculating the 3D dislocation density, using a measured thickness of the thin sections as $\sim 16.5 \times 10^{-6}$ m for the deformed sample and $\sim 9.9 \times 10^{10\ -6}$ m for SC-06, yields an apparent recovery rate for the light microscope study of 5.0×10^{-18} m^2 s^{-1}, comparable with the uncorrected 2D value, indicating that a much smaller depth of information determined for FE-SEM dislocation imaging has a greater effect on calculating k (see Appendix).

The rate constant of dislocation density kinetics for the light microscope study is one order of magnitude higher than the recovery rate from the analysis using high magnification FE-SEM images. This suggests that the difference lies in the capacity of the latter technique to resolve a higher number of individual dislocations. The higher FE-SEM dislocation densities, which apply equally to ρ_f and ρ_i, translate directly into lower recovery rates through Eq. 4.

It is interesting to note that the rate constant from the SEM study by Karato et al. (1993) is lower by one order of magnitude than the Karato and Ogawa (1982) LM study, also consistent with the notion that more dislocations were counted at higher resolution. Karato et al. (1993) propose that their focus on a particular slip system was the cause for a lower recovery rate and that the thermodynamic environment may also be important, including silica activity, which was controlled by an opx buffer in their study. The former might be possible, but should be investigated further. The latter is unlikely, however, because opx buffering was also used in the present study for sol–gel olivine. The silica activity was not deliberately fixed for the San Carlos olivine of the present study. However, microstructural analysis does not indicate the presence of MgO and previous analysis showed some 1–2% opx in the same material (Jackson et al. 2002). Therefore, opx-buffering may have contributed to lower recovery rates in Karato et al. (1993) and in our study but was unlikely to be the only contributing factor.

The difference between an uncorrected 2D and a corrected 3D dislocation density calculation from Tables 1 and 2 would produce up to half an order of magnitude increase in recovery rate if k had been calculated from 2D densities. This may contribute towards an explanation for a lower recovery rate in this study using the 3D results. Unfortunately, previous results cannot be simply recalculated to a 3D result because the raw images were required to measure the dislocation lengths[1]. The depth of information will also be different depending on the accelerating voltage used in SEM or section thickness for LM and TEM studies. It is not known whether previous dislocation densities were given a geometric correction of the type $\rho_{3D} = 2(N/A)$ where N is the number of dislocations and A the area (Karato 2008). Nonetheless, this correction is only an assumption because dislocations in olivine are not randomly oriented but confined to the slip systems in olivine on which they multiply. The large errors produced by this calculation can be reduced if the total length of dislocation lines for a given volume is measured (Karato and Jung 2003), as done in this study.

Finally, Karato and Sato (1982) have shown there may be an effect of oxygen fugacity on dislocation recovery. However, results from two experiments labelled Fo-08 and Fo-08* (Table 1 and 50 h curve for 1,200°C in Fig. 5), separated by over one order of magnitude in f_{O_2} are indistinguishable within uncertainty.

Recovery mechanisms

Static dislocation recovery is driven by the reduction in the strain energy within and possibly between grains. It is commonly believed that dislocations in olivine can migrate at high temperature via two mechanisms—glide, climb or a combination of both—when no external stress is applied. Obstacles to dislocation glide may be interstitial atoms, trace elements or other dislocations, all of which could need to be overcome by dislocation climb requiring the diffusion of Si, O, Mg, and Fe but controlled by the slowest species, Si (Dohmen et al. 2002). While both glide and climb are enhanced at higher temperatures, the temperature dependence for glide is not as high as for climb. Therefore, at higher temperature, dislocations of opposite sign that are attracted to each other through glide are subsequently capable to climb over obstacles to annihilate. Either climb or glide is the rate limiting step controlling dislocation recovery.

The dislocation structures observed in the deformed polycrystalline olivine samples, #6532 (sol–gel) and #6701 (San Carlos), are quite similar to structures seen in natural single crystal olivine that underwent dislocation creep (e.g. Durham et al. 1977; Bai and Kohlstedt 1992). Some of the recovered dislocation sub-structures such as dislocation walls are also comparable to those in annealed specimens from previous studies (Bai and Kohlstedt 1992, Fig. 11 and Karato and Ogawa 1982). The similarities indicate that the dislocation creep and recovery mechanics are comparable for all olivine materials.

The activation energies for dislocation recovery determined in all the investigations of San Carlos olivine are very similar around 350 kJ mol^{-1} whereas sol–gel olivine has an activation energy of $\sim$240 kJ mol^{-1} and therefore a less pronounced temperature dependence of the rate constant. However, this lower activation energy is not associated with a higher recovery rate (Fig. 4). With an absence of impurity defects in our sol–gel olivine (c.f. Al, Mn and Cr as detected in San Carlos olivine; Spandler and O'Neill 2010), one might have expected greater mobility of dislocations and a larger value for the recovery rate during annealing compared with San Carlos, especially towards lower temperatures where glide is more important. Since this was not observed, impurity defects were apparently not limiting the rate of dislocation recovery.

Recovery could also depend on whether dislocations are dominated by an edge or screw character, affecting dislocation recovery kinetics via differences in the nature and behaviour of jogs and kinks. A straight dislocation segment also undoubtedly behaves differently from a curved segment. In most cases, dislocations were of mixed nature and at least gently curved. Free dislocations tend to be mostly of screw character with relatively long straight segments consisting both of [001] and [100] Burgers vectors as previously observed in sol–gel olivine (Faul et al. 2010, see Fig. 7c). Only in one single crystal study was a particular slip system in olivine controlled and investigated (Karato et al. 1993). The other single crystal data potentially involve multiple slip systems. It is not clear, however, why the dominant easy slip system in olivine, (010)[100], would actually contribute to a lower rate constant as measured by Karato et al. (1993), unless single crystals only produce one dominant type of dislocation which therefore does not become entangled during annealing. The high initial dislocation densities in this study could conceivably reduce the recovery rate by initial entanglement of dislocations.

One other factor which may relate to the low measured recovery rates is the small grain size of our polycrystals. The way dislocations interact with each other in the presence of grain boundaries remains largely unknown. However, small grain size might affect the overall dislocation mobility via back-stress as embedded in the Hall-Petch relation (see e.g. Hall 1951; Hull and Bacon 2001). In addition, plastic deformation is characterised by the heterogeneous distribution of dislocations in grains and their

[1] Raw images from this study are available upon request.

participation in strain avalanches (Csikor et al. 2007). Consequently, understanding dislocation interactions with grain boundaries is critical to understanding crystal plasticity and recovery. The dislocation recovery mechanism in the relatively fine-grained materials in this study might involve a higher internal resistance from grain boundaries that complicates glide, climb and annihilation of dislocations not seen in single crystal olivine experiments. For instance it could be that residual internal stresses act as long range obstacles to easy dislocation mobility within grains during annealing at high temperature. In addition, dislocation arrangements (e.g. tilt walls) within grains also tend to screen long range stress fields (Moretti et al. 2008).

Dislocation recovery related to diffusion experiments and creep

If dislocation climb is the dominant recovery process, then dislocation recovery kinetics would be related to diffusion rates of the appropriate species in olivine. Studies of electrical conductivity in olivine suggest that magnesium vacancies and small polarons ($Fe^{\cdot}_{Mg}$) are the major charge carriers and that silicon interstitials are the slowest diffusing species (Smyth and Stocker 1975; Roberts and Tyburczy 1993; Du Frane et al. 2005). Single crystal olivine diffusion experiments have shown that Fe–Mg diffusion (Jaoul et al. 1995; Chakraborty 1997; Dohmen et al. 2007) is the fastest followed by oxygen (Jaoul et al. 1980; Reddy et al. 1980; Gerard and Jaoul 1989), and finally silicon (Houlier et al. 1988, 1990; Dohmen et al. 2002). For temperatures between 1,300 and 1,500°C. Dohmen and Chakraborty (2007) reports Fe–Mg diffusion coefficients ($\log_{10}D$, $m^2\ s^{-1}$) between −16 and −15 and Dohmen et al. (2002) reports oxygen diffusion coefficients ranging between −19.5 and −18, whereas silicon diffusion coefficients range between $\log_{10}D = -21.5$ and −19.5. Karato and Ogawa (1982) suggested that the rate constant, k can be related to the diffusivity, D as

$$k = \alpha' D \tag{7}$$

where α' is approximately 300. For more explanation of the terms, including the value for α, see the appendix of Karato and Ogawa (1982). The assumptions for this derived equation are that all dislocations will form dislocation dipoles and annihilate (second order kinetics), that the mean distance of dislocations is proportional to the mean distance of the dislocation pair, that a Weertman climb-controlled creep mechanism operates and that jogs are saturated with vacancies. With this equation, our measurements of k indicate diffusion coefficients close to that for oxygen. At 1,400°C a value of −21.25 ($\log_{10}D$, $m^2\ s^{-1}$) for the silicon diffusion coefficient would yield an equivalent value of −18.77 for the rate constant of dislocation recovery, roughly two orders of magnitude slower than observed in this study.

In addition, other studies have established that E_{creep} is similar to E_{diff} for Si diffusion in dry single crystal olivine (e.g. E_{creep} = 523 kJ mol^{-1}, Goetze 1978 and E_{diff} = 529 kJ mol^{-1}, Dohmen et al. 2002) and polycrystalline sol–gel olivine (484 kJ mol^{-1}, Faul and Jackson 2007). This activation energy is much higher than the one obtained from static dislocation recovery experiments in the present and previous studies. A lower value of 358 ± 28 kJ mol^{-1} was reported for silicon diffusion in water-bearing olivine with ~45 ppm H_2O (Costa and Chakraborty 2008). However, Fourier Transform Infrared Spectroscopy (FTIR) showed no water was present in the sol–gel olivine, whereas 423 H/10^6 Si (~26 wt. ppm H_2O) was measured in the San Carlos specimen. Overall, this complicates any comparison between static recovery and creep in olivine and the mechanism for dislocation recovery remains unclear.

Implications for high temperature experimentation

This study was motivated by the need to have a stable dislocation density during planned high temperature forced oscillation measurements of seismic wave attenuation on olivine polycrystals hot-pressed from either sol–gel or San Carlos derived precursor powders. We conclude that the temperature should not exceed 1,100°C if the dislocation density is to be maintained within 20% throughout prolonged (~50 h) attenuation measurements (Fig. 5) from the dislocation recovery kinetics of the present study. Higher temperature experiments of dislocation damping in pre-deformed single crystal forsterite by Gueguen et al. (1989) may have been complicated by substantial dislocation recovery. For example, a 20% reduction in dislocation density would be expected after only 1 h at 1,400°C (Fig. 5), the maximum temperature for the attenuation experiments of (Gueguen et al. 1989). Larger rate constants for the single crystal olivine (comparable to Karato et al. 1993) would imply even more rapid changes in dislocation density.

Conclusion

In this study, samples of polycrystalline olivine, hot-pressed from either sol–gel or natural San Carlos precursor powders have been deformed and annealed under a controlled atmosphere at various temperatures up to 1,500°C. The observed decrease in dislocation density as a function of temperature and time is adequately described by an empirical second order law for dislocation recovery kinetics. The associated activation energy for dislocation

recovery under static conditions is 240 ± 43 kJ mol^{-1} for sol–gel olivine and and 355 ± 81 kJ mol^{-1} for San Carlos olivine.

In this study, a new and consistent method for estimating the 3D dislocation density in iron-bearing olivine has been presented. This approach contributes half an order of magnitude increase in dislocation density and a corresponding decrease in recovery rate. The uncertainty in the imaging depth, d should be noted however and further work is required to refine its value.

The recovery rates for both data sets are markedly lower compared to previous studies on single crystals by 1–2 orders of magnitude. This discrepancy could be partly related to the imaging techniques used by the various authors: LM, TEM and SEM as opposed to a high resolution FE-SEM in this study. It has been demonstrated that imaging dislocations using the LM at 1,000× will count only ∼1% of the dislocations imaged by FE-SEM at 8,000×. This causes an apparent increase of about two orders of magnitude of the rate constant for dislocation recovery. In addition, there may be an effect of grain size on the rate constant, where fine-grained aggregates have higher internal back-stresses exerted on the grain boundaries, slowing down dislocation (glide) kinetics. However, the sol–gel and San Carlos olivines of significantly different grain size is at best marginally resolvable.

Microstructural analysis reveals dislocation re-organisations including straightening of dislocations and formation of tilt walls that accompany the reduction in free dislocation density. While it is not clear if there is a particular species of vacancy responsible for controlling dislocation climb, it appears to be controlled by fast diffusing oxygen. The commonly assumed slowest diffusing species in olivine, Si appears not to control the static dislocation recovery rate.

Acknowledgments We would like to thank Craig Saint for his assistance in the laboratory and Frank Brink at the Electron Microscopy Unit. This research was funded by the EIPRS grant from the Australian government. The manuscript was greatly improved by Dr. Ralf Dohmen and an anonymous reviewer.

Appendix

The electron penetration depth and depth of information, d can be approximated using Monte Carlo (MC) electron interaction simulations. The programme used here is called CASINO and is free to use (http://www.gel.usherbrooke.ca/casino/) and its operation is summarized by Drouin et al. (2007).

The electron penetration depth value depends on three variables; the sample density, accelerating voltage and sample composition. These are related to each other through the equation derived by Kanaya and Okayama (1972), as restated by Goldstein et al. (1984).

$$R_{KO} = 0.0276AE_0^{1.67}/(Z^{0.889}\rho) \quad (8)$$

where R_{KO} is the electron penetration depth in, μm is the target density in g/cm^3 is the electron accelerating voltage in keV, Z is the average atomic number of the target and A, the average atomic mass is in g/mol. The calculated depth of information, d (see Eq. 1) is approximately 0.3 of the R_{KO} range (Goldstein et al. 1984, pp. 72–89).

The depth of information relates to the interaction volume for BSEs which return to the sample surface through elastic collisions, then escape to land on the BSE detector. However, there much uncertainty in estimating the maximum depth from which the majority of BSEs returned. Not all electrons return back to the detector, especially electrons escaping at high angles. Also BSE electrons which interact with the iron oxide precipitates at dislocations might need to be described by a different d.

The problem was addressed experimentally by Karato and Lee (1999) by taking a single crystal olivine in the $[101]_c$ orientation and deforming it so that the (001)[100] and the (100)[001] slip systems were both activated. When the crystal was cut along the (010) plane, the dislocation lines made an angle of 45° to this surface and the 'effective thickness,' or depth of information was calculated from the apparent length of lines in the SEM images on the assumption that all dislocations were straight and parallel to one of the shear directions. The authors obtained a result of (0.9 ± 0.1) $\times 10^{-6}$ for 15 keV BSEs which was later refined to a lower value of $\sim 0.6 \times 10_{-6}$ (personal communication, Prof. Shun Karato 2009). Equation 1 predicts a maximum electron penetration depth of 1.99×10^{-6} for Fo_{90} at 15 kV (with 3.3 g/cm^3 specimen density). The Monte Carlo approach predicts a maximum depth of information for BSEs of about $d \approx 0.62 \times 10^{-6}$ m, which is not too far off the measured value after applying the 0.3 factor predicted by Goldstein et al. (1984).

In this study, a lower accelerating voltage of 5 kV was used to limit the imaging of dislocation lines to a thinner surface layer (Figs. 2 and 6). The geometry of dislocations is less discernible but measuring the length and number of dislocations was more reliable because dislocation overlap is lessened. Unfortunately, in this study we do not have a 'calibration' specimen of the type employed by Karato and Lee (1999) to calibrate a depth value for the backscattered-electron imaging. Using Eq. 8 at 5 kV, R_{KO} = 0.32 μm. This is supported by running a Monte Carlo simulation (Fig. 6a) which also predicts a depth of information for BSEs of $d \approx 0.095$ μm with the factor from Goldstein et al. (1984) of $d \sim 0.3R_{KO}$.

Figure 6 illustrates clearly that the depth sampled by BSEs is very dependent on the accelerating voltage. The

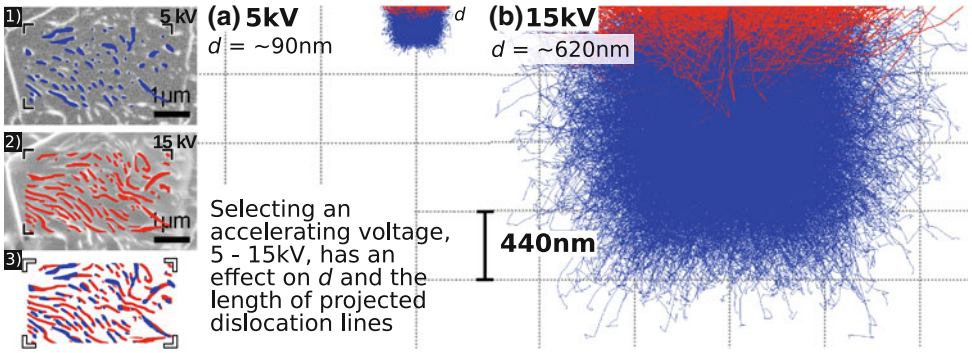

Fig. 6 Monte Carlo electron interaction simulations at (**a**) 5 kV and (**b**) 15 kV accelerating voltage for a solid with composition and density of Fo_{90}. The *red lines* represent the backscattered electron paths. The value for depth of information at 95% confidence interval is shown in *bold* on the vertical scale in each case. The *blue lines* indicate the travel paths for the primary electrons that change direction due to elastic scattering events. Both simulations are shown at the same scale for comparison. The *inset* shows a comparison between 5 and 15 kV accelerating voltage with maximum contrast for the same region. Note that the dislocations in (*2*) are longer and that some sets of dislocations can be found which are not present in (*1*). (*3*) shows the comparison of hand-traced dislocations in the area highlighted by the *dislocation lines* in (*1*) and (*2*)

depth of information from the Monte Carlo simulations, for both incident energies, can be combined with the measured projected lengths, l to calculate 3D dislocation densities. These can then be compared for consistency at different accelerating voltages. The dislocation density of the FE-SEM images in the inset of Fig. 6 was obtained, not via the usual process of filtering, but via hand-tracing each dislocation line to avoid any artefacts that result from applying a series of contrast filters. The first large grain measured at both 5 and 15 kV indicates a ratio for l_0 to be 1:2 for a consistent dislocation density. The next grain measured a ratio of 1:1.7 for l_0 and a third gave a ratio of 1:1.9 for l_0. A higher ratio of l_0 at 5 to 15 kV implies an equivalent higher ratio of d between 5 and 15 kV. The measurements differ significantly from both the ratio from the Monte Carlo simulations (95/600 = 1/6) and the prediction from Eq. 1 $(5/15)^{1.67} = \sim 0.16$.

There are several complications that may explain this. Firstly, the atomic number of the decorated dislocation lines (iron oxides) is far higher than the enclosing olivine which reduces the electron penetration depth. To simulate this accurately, one would need complex electron interaction models like those of Hennig and Denk (2007). Secondly, there are also considerations related to the acceptance angle of the BSE detector and the escape-angle distribution of BSEs (Murata, 1976; Goldstein et al. 1984). BSEs notably emerge from the surface of the specimen away from the primary electron source area due to changes in travel directions from elastic collisions in the material. The further out, the less energy the BSE generally has. Therefore, it is preferable for highest image resolution to select only the high energy BSEs. In addition, the escape probability of a BSE decreases gradually with penetration depth. There is no cut off value. This means that a single value cannot accurately define the depth of information (Goldstein et al. 1984). One must also take into account that the ratios of l_0, calculated from 5 and 15 kV BSE images, are a lower estimate because at higher kV the dislocations overlap significantly which makes it very difficult to draw the entire length of each dislocation.

Lastly, the measured value of l appears to have a small effect on the calculated recovery rate and activation energy. For example, at 1,450°C with $d = 0.095$ μm, $k = 9.9 \times 10^{-18}$ m^2 s^{-1}. With $d = 0.3$ μm, $k = 3.4 \times 10^{-17}$ m^2 s^{-1}. This effect is related to the fraction of short dislocations for which l approaches d. When there is a large fraction of long dislocations, the dependence on d is greater (i.e. shorter d produces relatively higher ρ_f and therefore lower k). For dislocations approaching 1 μm in length, d can be effectively ignored. The way k is correlated with d and the length distribution of dislocations imaged in each experiment points to the high uncertainty in E_a. Despite all this, however, using a depth of information, $d = 0.095$ μm, is still a good approximation for obtaining an accurate estimate of the 3D dislocation density.

References

Bai Q, Kohlstedt DL (1992) High-temperature creep of olivine single-crystals 2. Dislocation-structures. Tectonophysics 206(1–2):1–29

Chakraborty S (1997) Rates and mechanisms of Fe-Mg interdiffusion in olivine at 980–1300°C. J Geophys Res 102(B2):12317–12331

Costa F, Chakraborty S (2008) The effect of water on Si and O diffusion rates in olivine and implications for transport properties and processes in the upper mantle. Phys Earth Planet Inter 166:11–29

Csikor FF, Motz C, Weygand D, Zaiser M, Zapperi S (2007) Dislocation avalanches, strain bursts, and the problem of plastic forming at the micrometer scale. Science 318(5848):251–254

Dohmen R, Chakraborty S (2007) Fe–Mg diffusion in olivine II: point defect chemistry, change of diffusion mechanisms and a model for calculation of diffusion coefficients in natural olivine. Phys Chem Miner 34:409–430
Dohmen R, Chakraborty S, Becker H (2002) Si and O diffusion in olivine and implications for characterizing plastic flow in the mantle. Geophys Res Lett 29
Dohmen R, Becker H, Chakraborty S (2007) Fe - Mg diffusion in olivine I: experimental determination between 700 and 1,200°C as a function of composition, crystal orientation and oxygen fugacity. Phys Chem Miner 34:389–407
Drouin D, Couture AR, Joly D, Tastet X, Aimez V, Gauvin R (2007) CASINO V2.42–a fast and easy-to-use modeling tool for scanning electron microscopy and microanalysis users, vol 29. Wiley Periodicals, USA, pp 92–101
Du Frane WL, Roberts JJ, Toffelmier DA, Tyburczy JA (2005) Anisotropy of electrical conductivity in dry olivine. Geophys Res Lett 32(24):L24,315
Durham WB, Goetze C, Blake B (1977) Plastic flow of oriented single crystals of olivine: 2. Observations and interpretation of the dislocation theory. J Geophys Res 82:5755–5770
Faul UH, Jackson I (2007) Diffusion creep of dry, melt-free olivine. J Geophys Res 112:1–14
Faul UH, Fitz Gerald JD, Farla RJM, Ahlefeldt R, Jackson I (2010) Dislocation creep of fine-grained olivine. J Geophys Res
Gerard O, Jaoul O (1989) Oxygen diffusion in San Carlos olivine. J Geophys Res 94(B4):4119–4128
Goetze C (1978) Mechanisms of creep in olivine. Philos Trans R Soc Lond 288(1350):99–119
Goetze C, Kohlstedt DL (1973) Laboratory study of dislocation climb and diffusion in olivine. J Geophys Res 78(26):5961–5971
Goldstein JI, Newbury DE, Echlin P, Joy DC, Fiori C, Lifshin E (1984) Scanning electron microscopy and x-ray analysis. Plenum Press, New York
Gueguen Y, Darot M, Mazot P, Woirgard J (1989) Q^{-1} of forsterite single crystals. Phys Earth Planet Inter 55(3-4):254–258
Hall EO (1951) The deformation and ageing of mild steel: Iii discussion of results. Proc Phys Soc Sect B 64(9):747. http://stacks.iop.org/0370-1301/64/i=9/a=303
Hennig P, Denk W (2007) Point-spread functions for backscattered imaging in the scanning electron microscope. J Appl Phys 102:1–8
Houlier B, Jaoul O, Abel F, Liebermann RC (1988) Oxygen and silicon self-diffusion in natural olivine at t = 1,300°C. Phys Earth Planet Inter 50(3):240–250
Houlier B, Cheraghmakani M, Jaoul O (1990) Silicon diffusion in San Carlos olivine. Phys Earth Planet Interiors 62:329–340
Hull D, Bacon DJ (2001) Introduction to dislocations, 4th edn. Butterworth-Heinemann, Oxford
Jackson I, Fitz Gerald JD, Faul UH, Tan BH (2002) Grain-size sensitive seismic wave attenuation in polycrystalline olivine. J Geophys Res 107(B12):2360
Jackson I, Faul UH, Fitz Gerald JD, Tan BH (2004) Shear wave attenuation and dispersion in melt-bearing olivine polycrystals: 1. specimen fabrication and mechanical testing. J Geophys Res 109(B6):B06201
Jaoul O, Froidevaux C, Durham WB, Michaut M (1980) Oxygen self-diffusion in forsterite—implications for the high-temperature creep mechanism. Earth Planet Sci Lett 47(3):391–397
Jaoul O, Bertranalvarez Y, Liebermann RC, Price GD (1995) Fe-Mg interdiffusion in olivine up to 9 GPa at T = 600–900°C; experimental data and comparison with defect calculations. Phys Earth Planet Inter 89(3–4):199–218
Jung H, Karato S (2001) Effects of water on dynamically recrystallized grain-size of olivine. J Struct Geol 23(9):1337–1344
Kanaya K, Okayama S (1972) Penetration and energy-loss theory in solid targets. J Phys D Appl Phys 5:43–58
Karato S (1987) Scanning electron microscope observation of dislocations in olivine. Phys Chem Miner 14(3):245–248
Karato S (2003) Mapping water content in the upper mantle. In: Inside the subduction factory, vol 138. AGU Geophysical Monograph Series, pp 135–152
Karato S (2008) Deformation of earth materials: an introduction to the rheology of solid earth. Cambridge University Press, London
Karato S, Jung H (2003) Effects of pressure on high-temperature dislocation creep in olivine. Philos Mag 83(3):401–414
Karato S, Lee KH (1999) Stress-strain distribution in deformed olivine aggregates: inference from microstructural observations and implications for texture development. In: Proceedings of the twelfth international conference on textures of materials, pp 1546–1555
Karato S, Ogawa M (1982) High-pressure recovery of olivine—implications for creep mechanisms and creep activation volume. Phys Earth Planet Inter 28(2):102–117
Karato S, Sato H (1982) Effect of oxygen partial-pressure on the dislocation recovery in olivine—a new constraint on creep mechanisms. Phys Earth Planet Inter 28(4):312–319
Karato S, Rubie DC, Yan H (1993) Dislocation recovery in olivine under deep upper-mantle conditions—implications for creep and diffusion. J Geophys Res 98(B6):9761–9768
Kohlstedt DL, Goetze C, Durham WB, Vandersande J (1976) New technique for decorating dislocations in olivine. Science 191(4231):1045–1046
Kohlstedt DL, Nichols HPK, Hornack P (1980) The effect of pressure on the rate of dislocation recovery in olivine. J Geophys Res 85(B6):3122–3130
Lui M, Evans B (1997) Dislocation recovery kinetics in single-crystal calcite. J Geophys Res 102(B11):24801–24809
McDonnell RD, Spiers CJ, Peach CJ (2002) Fabrication of dense forsterite-enstatite polycrystals for experimental studies. Phys Chem Miner 29(1):19–31
Mei S, Kohlstedt DL (2000) Influence of water on plastic deformation of olivine aggregates. 1: Diffusion creep regime. J Geophys Res 105(B9):21457–21469
Moretti P, Laurson L, Alava MJ (2008) Dislocation interactions mediated by grain boundaries. Condens Matter Mater Sci 0803.1136:1–13
Murata K (1976) Exit angle dependence of penetration depth of backscattered electrons in the scanning electron microscope. Phys Solid State 36:197–208
Nes E (1995) Recovery revisited. Acta Metall Mater 43:2189–2207
Poirier JP, Vergobbi B (1978) Splitting of dislocations in olivine, cross-slip-controlled creep and mantle rheology. Phys Earth Planet Inter 16:370–378
Reddy KPR, Oh SM, Major LD, Cooper AR (1980) Oxygen diffusion in forsterite. J Geophys Res 85:322–326
Roberts JJ, Tyburczy JA (1993) Frequency-dependent electrical-properties of dunite as functions of temperature and oxygen fugacity. Phys Chem Miner 19(8):545–561
Smyth DM, Stocker RL (1975) Point defects and nonstoichiometry in forsterite. Phys Earth Planet Inter 10(2):183–192
Spandler C, O'Neill HS (2010) Diffusion and partition coefficients of minor and trace elements in San Carlos olivine at 1,300°C with some geochemical implications. Contrib Miner Petrol 159: 791–818
Tan BH, Jackson I, Fitz Gerald JD (2001) High-temperature viscoelasticity of fine-grained polycrystalline olivine. Phys Chem Miner 28(9):641–664
Yan H (1992) Dislocation recovery in olivine. Master's thesis, University of Minnesota